Case Study

# Study of time- and distance-dependent degradations of network RTK performance at high latitudes in Norway

Knut Stanley Jacobsen[1] · Nadezda Sokolova[2] · Mohammed Ouassou[1] · Anders Martin Solberg[1]

© The Author(s) 2023     OPEN

## Abstract

In this study we examine the performance of a network real-time kinematic (NRTK) positioning service at high latitudes ($\approx 70^{\circ}$ N). The NRTK used is the Norwegian national positioning service "CPOS". To test the performance, 6 geodetic quality receivers were deployed at various distances from the network receivers and used to collect positioning data for most of the year 2021. This test network is located in the night-time auroral oval region during normal conditions. Statistics are presented showing variation in performance as a function of the distance to the nearest NRTK receiver and as a function of the time-of-day. Performance is found to be significantly degraded during night-time, with approximately ten-fold increases of the occurrence of large positioning errors and significant increases in the time-to-fix. The distance from the network was also found to be a factor for significant performance degradation, with approximately ten-fold increases in the occurrence of large positioning errors when comparing results from a receiver close to the network (1.2 km) to a receiver a moderate distance away (11.5 km). The cause of the observed degradations are likely small-scale ionospheric density structures in the auroral oval region. Observational evidence of such gradients is shown.

## Article highlights

- Professional satellite positioning services in the vicinity of the auroral oval region are frequently degraded during night-time.

- The distance between the user and the closest network receiver site is an important factor for the severity of the degradations, even at distances of only a few km.
- The cause of the disturbances are likely ionospheric structures related to activity in the auroral oval region.

Keywords  GNSS · Network RTK · High latitude · Ionospheric gradients

✉ Knut Stanley Jacobsen, knut.stanley.jacobsen@kartverket.no | [1]Geodetic Institute, Norwegian Mapping Authority, Hønefoss, Norway. [2]Sustainable Communication Technologies, SINTEF, Trondheim, Norway.

SN Applied Sciences
A SPRINGER NATURE journal

# 1 Introduction

Network real-time kinematic (NRTK) positioning is a refinement of real-time kinematic (RTK) positioning. In RTK, a single reference receiver is used, and a user receiver located nearby this reference receiver can almost eliminate all spatially correlated errors (e.g. satellite position errors and tropospheric and ionospheric errors) through differencing of observations (user minus reference). However, the greater the distance is between the user receiver and the reference receiver (this distance is often referred to as the "baseline length"), the less correlated are e.g. the atmospheric errors between the two receivers, and consequently, the more difficult it is for the user receiver to resolve the phase ambiguities to the correct integers and thus obtain a high position accuracy. Traditionally, 10 km has been judged as an almost absolute maximal advisable baseline length for RTK. The NRTK technique was invented in order to mitigate these distance dependencies [1–4]. Algorithms were developed to take advantage of the network to provide more accurate corrections than what is possible from single reference receivers. [5, 6] developed a network adjustment method "NetAdjust" based on a least squares collocation spatial interpolation algorithm (specifically, a variant of this that is commonly referred to as *Kriging* [7–9]), and used this to compute improved user corrections. The algorithm uses covariance analysis to predict the user carrier-phase error statistics. The impact of baseline length on ambiguity resolution was also analyzed as part of the work. When collecting GNSS pseudorange and phase observation data from a cluster of several (at least three [10, ch 3.1]) reference receivers (here called network receivers) and processing them in a common processing centre, the spatially correlated errors can firstly be estimated at the network receivers and then interpolated between them. Based on such an interpolation, the processing centre can provide the user with synthetic observation data for the user's location, data which the user receiver can use in an ordinary RTK positioning algorithm (with differencing of observations). If the user is located inside the receiver network and the spatial structures of the atmospheric errors are not too small for the interpolation algorithms, the user receiver can be allowed to operate at a considerably larger distance from the closest network receiver in the NRTK case than the distance it could be allowed to operate on from the single reference receiver in the RTK case, and still achieve the same position accuracy.

The Norwegian Mapping Authority (NMA) operates a national network of GNSS receivers, which is used for positioning services and various studies. NMA provides a positioning service "CPOS" for mainland Norway, using the NRTK technique. Researchers at the NMA have previously studied the statistics of ionospheric disturbances and their correlation with GNSS positioning errors in [11], and published case studies on the effects of space weather events on GNSS in [12–14].

An important task of the NRTK system is to account for spatially-dependent biases due to the atmosphere. These can be divided into tropospheric delays and ionospheric delays. The spatially-dependent information is necessarily more correct closer to the network receivers, as any interpolation will inevitably differ from the actual reality. The difference between the interpolated corrections and the real atmospheric delays can be smaller or larger, depending upon the structure of the atmosphere. Variations that are large-scale (larger than network inter-station distances) and slow to change in time can be modeled with some confidence, while small-scale and/or rapid variations are much more difficult to model accurately.

There have been several studies performed on the variation in performance with distances from the reference receivers in RTK and NRTK setups (e.g. [15–18]). [19] developed a variance model for user accuracy in NRTK positioning as a function of baseline length by considering different techniques such as Virtual Reference Station (VRS) [3] and Flächen-Korrektur-Parameter (FKP) [20]. [21] show that baseline length between the rover and the closest reference station affects the horizontal and vertical precision. As the rover moves away from the closest reference station, precision decreases for both horizontal and vertical components.

The performance will depend on the geographical region, as the atmospheric conditions can vary substantially in different regions, and to some extent on the hardware and software used for the NRTK system. This study is based on data from a network at high latitudes ($\approx$ 70º N), in a region which is in the auroral zone at night-time. The auroral zone is known to have a greater degree of ionospheric activity and small structuring than the ionosphere at middle latitudes, even during conditions that are not flagged as a space weather event. There are several different processes that can structure the plasma in the auroral oval (See e.g. [22–26]), and the structured plasma has been directly linked to signal disturbances (e.g. [27–29]). The objective of this study is to characterize the impact of these kinds of variations during normal levels of activity (i.e. not focusing on events) on NRTK positioning at short-to-medium distances to the nearest network receiver.

Section 2 presents the data sources and Sect. 3 explains how the data have been processed. In Sect. 4, the results are presented and discussed. The conclusions are summarized in Sect. 5.

## 2 Data sources

NMA operates a nation-wide network RTK positioning service named "CPOS". The service is based on the Trimble Pivot Platform, which is a commercial software solution from Trimble Inc.. Details regarding its internal algorithms are not public information, but it can be considered as an industry standard implementation of network RTK algorithms.

The performance of the service is independently monitored by what we refer to as "RTK monitors". These are survey-grade GNSS receiver/antenna equipment setups that connect to the service in the same way as a normal user. The RTK monitors are managed using the "RTK-Mon" software developed by Martin Freitag (Landesamt für Vermessung und Geoinformation, SAPOS®-Bayern). Table 1 shows basic information about the monitor receivers.

RTKMon starts a measurement session each 60 s. When a session starts, the RTK monitor receiver will receive the correction data from the RTK server. This data stream continues until the receiver has reported 5 good (fixed ambiguities) solutions to RTKMon. Then, the RTK correction data stream to the monitor is switched off. The RTK monitor receiver will try to extrapolate the corrections in order to keep a fix solution for up to 30 s. Eventually the receiver will revert to a less accurate (floating ambiguities) solution, and later to an autonomous solution or no solution. The monitoring system tracks these different states, as well as the calculated coordinates every second. Under very bad conditions it may take a long time before a fixed solution can be found. When this happens RTKMon may extend a measurement session beyond its default length. The main objective for the periodic resets is to measure the time-to-fix (TTF), which is the time from the start of a RTKMon measurement period until the first coordinate solution with fixed ambiguities. Its lowest possible value is 1 s. Typical values for a user with good equipment and good environmental conditions are in the single digit seconds.

In addition to the measurement session data logged by RTKMon, raw positioning data are stored at full (1 s) resolution. The raw positioning data consist of timetags, coordinates and status flags.

Figure 1 shows the geographic positions of the monitor receivers and the NRTK (CPOS) receivers in the area. The distances between TRO1 and its immediately surrounding network receivers (HANC, OLDC, BALC, FINC, SOMM) are from 36 to 62 km. For this study, we use data from the whole year of 2021. The receivers TM01, TM03, TM04 and TM05 have been operating since the 26th April 2021, while MTRM and MSIM have been operating the
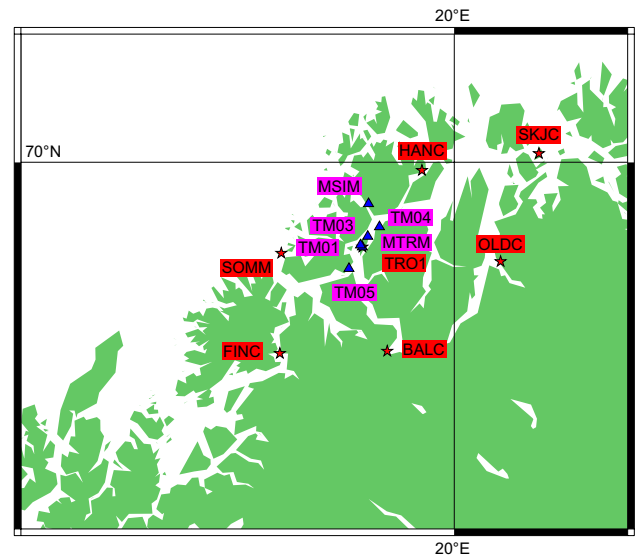


**Fig. 1** Geographic locations of the GNSS receivers. Red stars are RTK network receivers, while blue triangles are monitor receivers

**Table 1** Information about monitor receivers used and their distance from the closest network RTK receiver

| Receiver code | Receiver type | Antenna type | Distance from TRO1 |
|---|---|---|---|
| MTRM | TPS NET-G5 | TPSCR.G5 TPSH | 1.38 m |
| TM01 | Leica GR50 | LEIAR10 | 1.2 km |
| TM03 | Leica GR50 | LEIAR10 | 5.3 km |
| TM04 | Leica GR50 | LEIAR10 | 11.8 km |
| TM05 | Leica GR50 | LEIAR10 | 11.5 km |
| MSIM | TPS NET-G5 | TPSCR.G5 TPSH | 19.5 km |

entire year. The monitors are using data from the GPS, GLONASS and Galileo constellations when calculating their positions.

## 3 Method

All coordinate data used in this study are filtered to only include coordinates with a status of "RTK fixed", which means that the receiver reports that it is using a fixed ambiguities solution.

To define the position error, a "true" coordinate must be defined. The position error is the difference between the instantaneous coordinate and the "true" coordinate. The "true" coordinates are weekly static solutions computed using the Bernese software [30]. As the solutions from Bernese were in the global reference frame IGb14, while the CPOS service provides coordinates in the national reference frame EUREF89 (which is the same as the European

Terrestrial Reference System 1989 (ETRS89)), the solutions must be transformed in order to be compared. The transformation library "PROJ" [31] was used to perform the transformations. For the "TM0_" test monitor receivers, there were residual coordinate offsets present. The offsets were computed as the difference between the mean Bernese coordinate and the mean CPOS coordinate, over the entire time period where CPOS coordinates were available. The vertical coordinate time series were corrected by these offsets, whose magnitudes were 3.1, 0.4, 1.4 and 2.6 cm for TM01, TM03, TM04 and TM05. Horizontal offsets were generally smaller and were not corrected for. A constant offset for the entire time series is not a result of ionospheric disturbances or other atmospheric effects. Thus we do not need to know the exact reason for the offsets, which is likely a lack of calibration as these receivers are not as well calibrated as the operational receivers that contribute to positioning services. No offset corrections were applied for MTRM and MSIM.

The positioning data are split into intervals with length 300 s. Within each interval, the following measures of performance are calculated:

- Mean position error, separately in 3 dimensions (north, east and vertical in a local coordinate system)
- Standard deviation of position, separately in 3 dimensions. This will be referred to as the "Noise" in position.
- Mean time-to-fix (TTF) during the interval

The data from the 300-second intervals are further processed in different ways to produce statistics:

- Statistics by day: For each day, the 5th percentile, median and 95th percentile of the position error and the median and 95$^{th}$ percentile of the position noise are calculated.
- Statistics by time-of-day: For each hour of the day, the 5th percentile, median and 95th percentile of the position error, the median and 95th percentile of the position noise and the median, mean and 95th percentile of the TTF are calculated (using the entire dataset, not just a single day).
- Coarser statistics by time-of-day: For the time periods "Magnetic Night", "Magnetic Dawn", "Magnetic Day" and "Magnetic Dusk", probabilites for the position error, posision noise and TTF to have a small, moderate or large value are calculated. "Magnetic Night" is defined as 20 to 03 UTC, "Magnetic Dawn" as 03 to 08 UTC, "Magnetic Day" as 08 to 15 UTC and "Magnetic Dusk" as 15 to 20 UTC. The main reason for the choice of these time periods is to clearly distinguish the time spent in or near the night-side auroral oval ("Magnetic Night") from the time spent well away from it ("Magnetic Day")

The "Magnetic" prefix is used to clearly distinguish these from the definition of day/night based on the presence/absence of sunlight. Statistics are also calculated for the time periods "Darkness" and "Sunlight", which are defined by the Sun being below or above the horizon.

- Probability density functions of the position error and position noise.
- Statistics by distance to nearest network receiver: For the time periods "Magnetic Night" and "Magnetic Day", the median and 95th percentile of the position error and the median and 95th percentile of the position noise for each monitor receiver are calculated.

## 4 Observations and discussion

Figure 2 shows the daily statistics for MSIM in 2021. The plot shows that the errors we see in the statistics are not just from one or two strong events, but is a frequent feature throughout the year. The reason for this is that as the location is located in the auroral oval during normal conditions, even very modest levels of enhanced activity can result in disturbances. There appears to be a slightly higher occurrence of errors during the first and fourth quarter of the year, which may be related to the semi-annual "Russell-McPherron" effect [34], but without a multi-year dataset we do not feel confident to draw a firm conclusion regarding that.

Figure 3 shows the statistics by hour-of-day for the East, North and Vertical coordinates of TM03. Both position bias and noise are increased during night-time for all three directions, but are significantly more increased for the vertical direction. The figure is included to show that the horizontal coordinates behave similarly to the vertical coordinate, but with smaller values. This has also been manually verified for the other receivers. To limit the amount of figures and tables in this paper, the rest of the results focus only on the vertical coordinate.

Figure 4 shows the statistics by hour-of-day for the Vertical coordinates, for all monitor receivers. MTRM differs from the others by having almost completely flat graphs. Otherwise, the position errors increase at night and with distance from TRO1. The variation of the position errors as a function of time-of-day increases significantly for receivers far away from the network receiver. For MTRM, which is co-located with the network receiver TRO1, errors are generally very low and show no noticeable variation by time-of-day. For the rest of the monitor receivers, the errors are higher at night-time and higher for receivers further away from TRO1. This is consistent with being caused by small-scale ionospheric structures. At night this region is in the auroral zone, in which several processes can create and

**Fig. 2** Time series of daily statistics of position bias and noise for MSIM. Top panel: Median, 5th and 95th percentile of vertical position error. Bottom panel: Median and 95th percentile of vertical position standard deviation



**GNSS monitor MSIM (Simavika-monitor)**
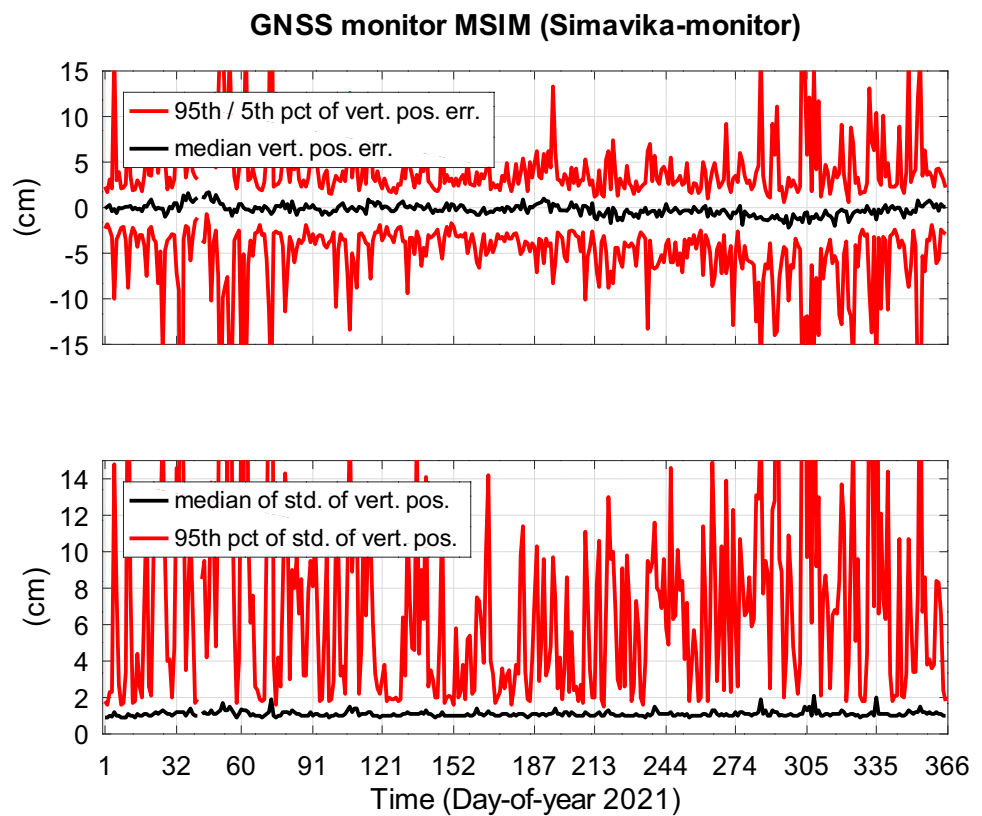
propagate density structures in the ionospheric plasma. This explains the timing of the enhanced errors. Errors that are increasing by distance from the network receiver in an NRTK service are a result of a mismatch between the real atmosphere and the modeled/interpolated atmosphere. As the variations of ionospheric density at scales smaller than the inter-station distances becomes stronger, it is expected that the errors in the interpolation will increase. The variation seen in Fig. 4 is smooth, and the period of enhanced activity is shorter than the period of low activity. A function with a cosine in its core, raised to a suitable power and with several offsets in different places of the equation, can mimic this shape. As an example, this function is similar to the top red line in the top panel:

$$f(Hour\ Of\ Day)$$
$$= 7\left(\frac{1}{2}\cos\left(\frac{2\pi(Hour\ Of\ Day + 2)}{24}\right) + \frac{1}{2}\right)^3 + 3. \quad (1)$$

We emphasize that this function is only intended as a rough illustration of the form of the functional relationship. It is not based on physical principles or properly fitted to the data.

To illustrate this, we have used the data from the same set of receivers as shown in Fig. 1 during a day with stronger ionospheric activity (18 October 2021) and studied spatial variation of the ionospheric delay.

The methodology and the tool used for this analysis are detailed in [32, 33]. Figures 5 and 6 show the spatial ionospheric gradient observed on the GPS PRN23 measurements by the NRTK station pairs and test receivers. As can be seen from Fig. 5, while the multiple of the NRTK station pairs do observe the spatial gradient, the magnitude of the observed ionospheric slope is lower compared to the observations made by the TRO1 and test receiver pairs that are separated by shorter distances. Another detail thought to make accurate interpolation more challenging during the periods of stronger ionospheric activity is the temporal decorrelation of the ionospheric slope observations introduced by the combined motion of the ionospheric wave front and the satellite's IPP velocity. This detail can be seen in Fig. 6, where the ionospheric wave front approaching the test network is observed first by TRO1-TM05 receiver pair, and then by TRO1-TM3, TRO1-TM04, and TRO1-MSIM respectively.

To check how well the daily pattern shown in Fig. 4 holds throughout the year Fig. 7 shows the hourly statistics for the 95th percentile of vertical position noise for the receiver MSIM, split by month. Lines show the times of sunset, sunrise and equinoxes. The major cause for disturbances of GNSS signals in this region is expected to be activity in the auroral oval region. This kind of activity is driven by the interaction between the solar wind and Earth's magnetic field and will thus vary with the magnetic
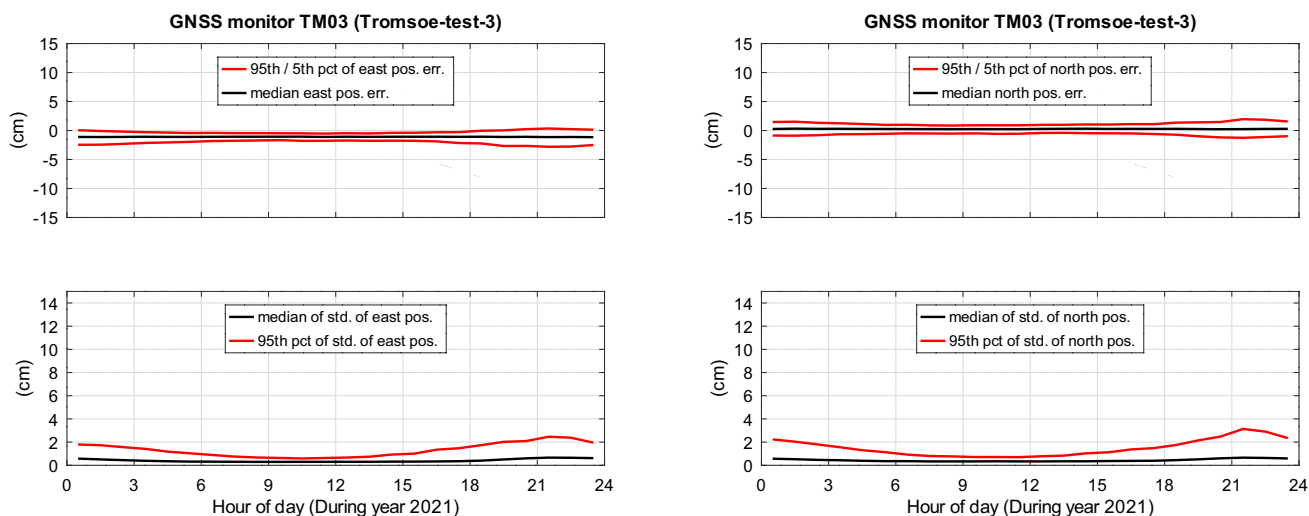
(a) East



(b) North
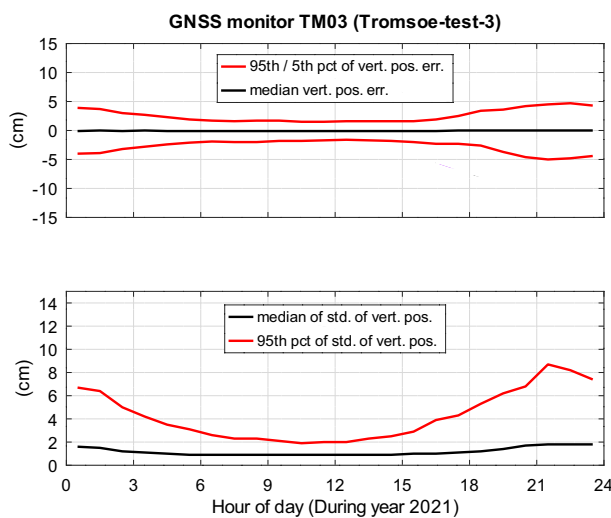


(c) Vertical

**Fig. 3** Statistics as a function of time-of-day for TM03, with a subplot for each coordinate axis (East/North/Vertical). Top panel of each subplot: Median, 5th and 95th percentile of position error.

Bottom panel of each subplot: Median and 95th percentile of position standard deviation

local time. (For a limited region and time period (i.e. less than decades), magnetic local time is equal to UTC plus an offset.) The high-latitude space weather impacts have a semi-annual variation, which can be explained by the modulation of reconnection processes by the variation of the tilt of the Earths magnetic field relative to the solar wind [34]. The hour-of-day has the strongest co-variation with the disturbance level, and the increased level of disturbances around the equinoxes is clearly seen in the figure. Whether the atmosphere is sunlit or not will modify the background conditions of the ionosphere, which may modulate the response of the ionosphere to the external

influence from space weather activity. We do not have sufficient data to clearly separate these contributions which are necessarily correlated as they all are functions of time. The general conclusion is that for all months there is more noise close to midnight than close to midday, with a similar shape of variation throughout the day, but the magnitude of the increased noise is lower during summer and highest near (+- 2 months) the equinoxes. The same general pattern is also true for the position errors and for the other monitor receivers, but with smaller magnitudes of the effect. Further analysis of these effects should be based on a multi-year dataset.

**Fig. 4** Statistics as a function of time-of-day. Top panel: 5th and 95th percentile of vertical position error. Bottom panel: 95th percentile of vertical position noise (standard deviation)
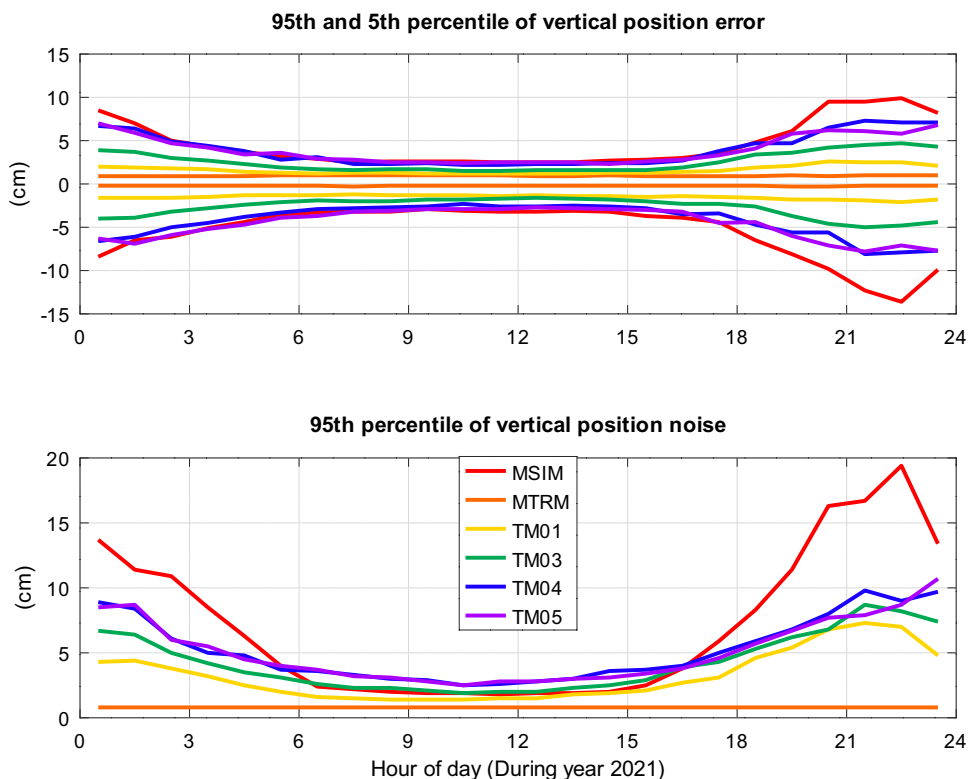


**Fig. 5** Spatial decorrelation of ionospheric delay observed on the GPS PRN23 based on the NRTK station pair data (station separation from 36 to 62 km)
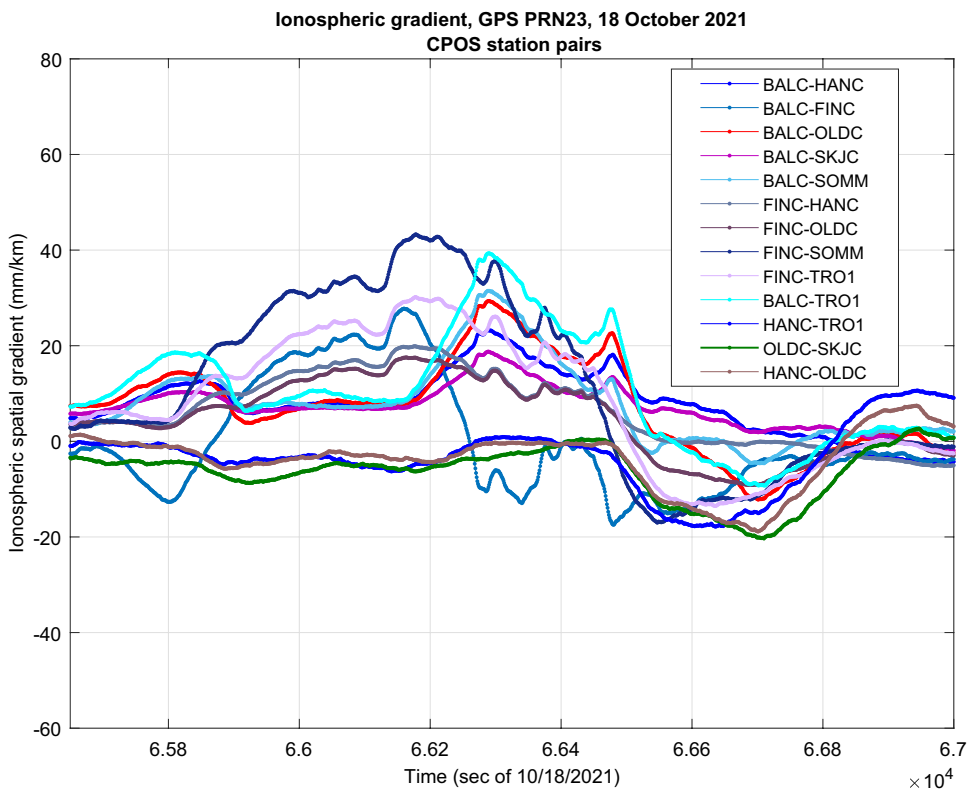
**Fig. 6** Spatial decorrelation of ionospheric delay observed on the GPS PRN23 based on the TRO1 station and test receiver data



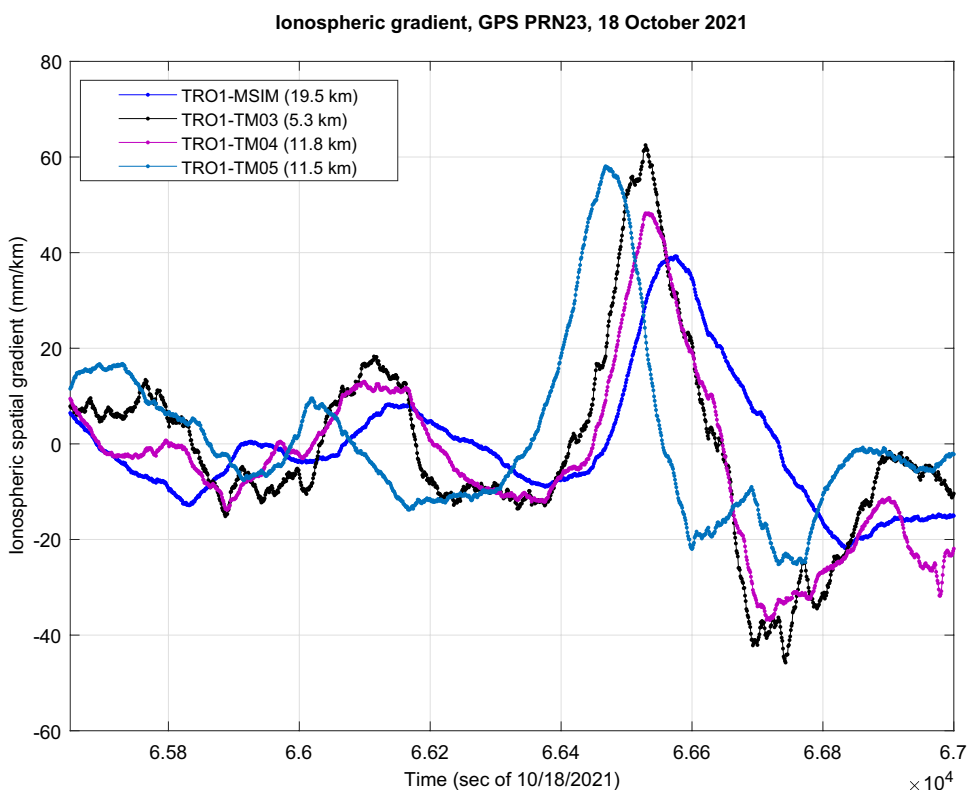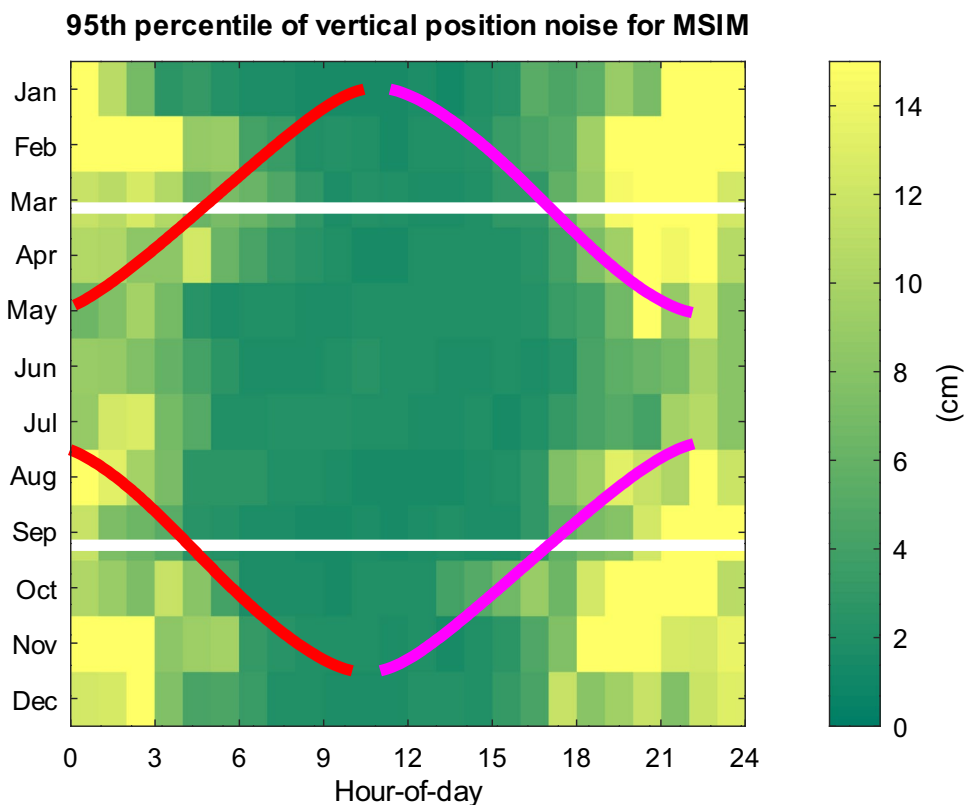Ionospheric gradient, GPS PRN23, 18 October 2021

**Fig. 7** 95th percentile of vertical position noise (standard deviation) depending on the month and hour-of-day. The red line marks sunrise, while the magenta line marks sunset. For days where the lines are not present, there is either permanent sunlight or darkness. The white dashed lines marks the equinoxes
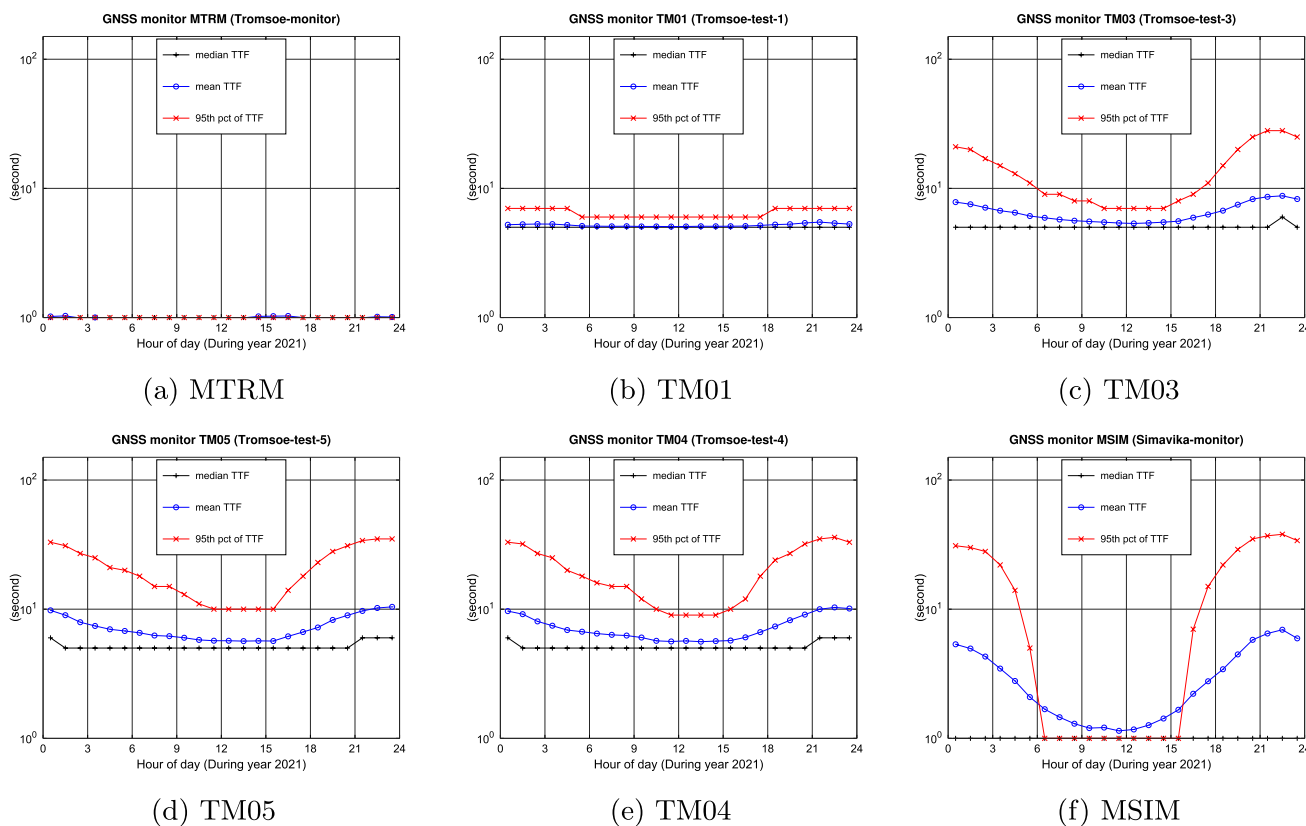


95th percentile of vertical position noise for MSIM

(a) MTRM                    (b) TM01                    (c) TM03



(d) TM05                    (e) TM04                    (f) MSIM

**Fig. 8** Statistics as a function of time-of-day, in a subplot for each monitor receiver. The plots shows the median, mean and 95th percentile of the time-to-fix

Figure 8 shows the statistics by hour-of-day for the time-to-fix, for all monitor receivers. The receivers are sorted by distance from the nearest network receiver, TRO1, in ascending order going left-to-right and top-to-bottom. For the contents of this plot the receiver type is important. The "TM0#" receivers are Leica GR50, while MTRM and MSIM are TPS NET-G5. The Leica receivers appear to have a hard-coded restriction that at least 5 s of data are required before reporting a fixed ambiguities solution. Thus their base level of time-to-fix is different from the Topcon receivers and their mean values are shifted slightly higher. The MTRM receiver almost always achieves an instant fix, while the other receivers show increased values at night and with distance from TRO1. TM01, at the distance of 1.2 km, shows a small increase at night-time, but the difference would likely not be noticeable for most applications. The other monitor receivers show greater increases, with their 95th percentiles peaking at several tens of seconds. At MSIM during day-time, the mean value is greater than the 95th percentile. In fact, both the median and 95th percentile are at the perfect 1 s value. This indicates that the data includes a small number of large spikes. In other words, its performance is generally good but has intermittent problems.
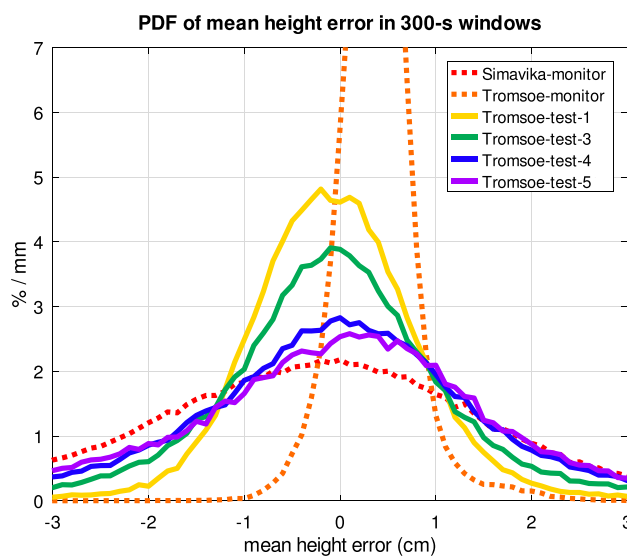


**Fig. 9** Probability density function of vertical position error, using the entire dataset for each receiver

Figure 9 shows the probability density functions of the vertical position errors for each receiver and Fig. 10 shows the probability density functions of the vertical
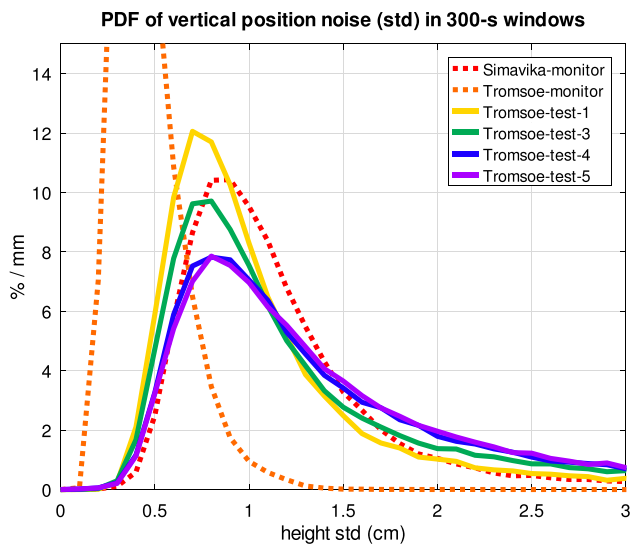
**Fig. 10** Probability density function of vertical position standard deviation, using the entire dataset for each receiver



**Fig. 11** Median and 95th percentile of absolute vertical position error as a function of distance to the nearest network receiver, for magnetic day-time (top panel) and magnetic night-time (bottom panel). The dashed lines are linear fits, with the fitted parameters reported in the legend

position noise for each receiver, based on the entire dataset. The receivers MTRM and MSIM are drawn with dotted lines to distinguish them from the rest because they are of a different receiver type and also have a longer time period of data, both of which could potentially influence the statistics. The probability density functions (PDFs) for vertical position errors clearly have a shape that depends on the distance from the network receiver. PDFs for the monitor receivers that are further away have a lower peak at zero error and larger values at the flanks. The position error PDF for MTRM is almost entirely within ± 1 cm, while the monitor receivers that are far away have distribution tails that extend far beyond the area shown in the plot. The PDFs for vertical position noise also clearly depend on the distance from the network receiver. The main features to notice in the plot are:

- Location of the peak of the distribution. For all receivers, including MSIM, the peak is located at higher values (further to the right in the plot) for receivers at a greater distance. The distributions all have a peak at the low end of their range of values, followed by a long tail.
- Height of the peak of the distribution. Apart from MSIM the height of the distribution peak is lower for receivers at greater distance, meaning that a lower portion of the noise values are at the low values.
- Distribution tails. Inversely to the previous points, receivers at a greater distance have a larger portion of the noise values at large values.
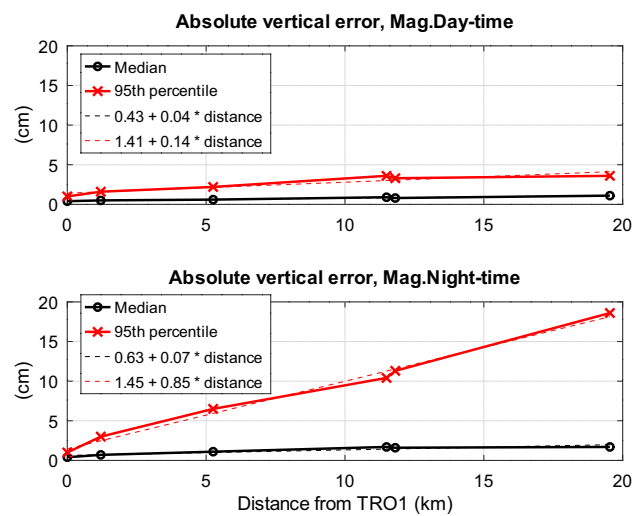
The reason that the PDF of MSIM does not fully match the pattern is likely a result of small differences in handling of noise by the hardware and/or firmware.

Figure 11 shows the median and 95th percentile of the absolute vertical position error as a function of distance to the nearest network receiver, for day-time (top panel) and night-time (bottom panel). All measures increase with
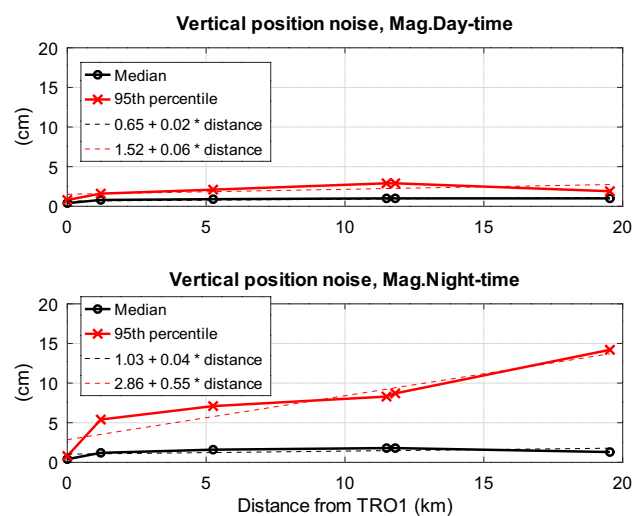


**Fig. 12** Median and 95th percentile of vertical position standard deviation as a function of distance to the nearest network receiver, for magnetic day-time (top panel) and magnetic night-time (bottom panel). The dashed lines are linear fits, with the fitted parameters reported in the legend

increasing distance, but the night-time 95th percentile has a particularly strong increase with distance.

Figure 12 shows the median and 95th percentile of the vertical position noise as a function of distance to the nearest network receiver, for day-time (top panel) and night-time (bottom panel). The night-time 95th percentile clearly increases with distance. The other measures show weaker signs of increase with distance.

Figures 11 and 12 show an overview of how the position errors increase with increasing distance from the network receiver. In general, all measures of positioning errors increase with increasing distance. However, the 95th percentile of both position error and noise have a much stronger response than the other measures. This can be understood as greatly enhanced tails of the distributions, or in other words that the occurrence rates of intermittent large errors is greatly increased. While the position errors are generally increased during night-time and at greater distance to the network receiver, the more practically significant difference is a greatly enhanced risk that a single measurement will have a large error.

Several tables present a different way to view the data, sorting the data for each monitor receiver by time of day and by small/moderate/large values, as specified in the tables. This way of presenting the statistics quantifies the amount of observations that have large errors/noise/TTF. Table 2 show the probabilities of the absolute vertical position error during magnetic "Night"/"Dawn"/"Day"/"Dusk" and during the time of sunlight or darkness to be in the categories "Less than 1 cm", "Between 1 and 5 cm" and "5 cm or greater". Table 3 show the probabilities of the vertical position noise during magnetic "Night"/"Dawn"/"Day"/"Dusk" and during the time of sunlight or darkness to be in the categories "Less than 1 cm", "Between 1 and 5 cm" and "5 cm or greater". Table 4 show the probabilities of the time-to-fix during magnetic "Night"/"Dawn"/"Day"/"Dusk" and during the time of sunlight or darkness to be in the categories "Less than 10 s", "Between 10 and 30 s" and "30 s or greater".

The tables for MTRM re-confirms its near-flawless performance in all parameters. The tables for the rest of the monitor receivers show again that performance is poorer at night-time and for receivers further away from the nearest network RTK receiver. In terms of the statistics for position errors of 5 cm or more, the increase from day-time to night-time was approximately tenfold. For TM01 (at 1.2 km distance) the increase in occurrence was from 0.3% to 2.0%, while for TM05 (at 11.5 km distance) it was from 2.3% to 14.7%. From those numbers we also see an approximate ten-fold increase in the

**Table 2** Probability for height error magnitude

| |posErr| | Mag.Night (%) | Mag.Dawn (%) | Mag.Day (%) | Mag.Dusk (%) | Darkness (%) | Sunlight (%) |
|---|---|---|---|---|---|---|
| Tromsø-monitor (MTRM) | | | | | | |
| < 1 cm | 95 | 95 | 95 | 95 | 92 | 97 |
| 1–5 cm | 5 | 5 | 5 | 5 | 8 | 3 |
| ≥ 5 cm | 0.0 | 0.0 | 0.0 | 0.0 | 0.0 | 0.0 |
| Tromsø-test-1 (TM01) | | | | | | |
| < 1 cm | 66 | 77 | 78 | 72 | 68 | 77 |
| 1–5 cm | 32 | 23 | 22 | 27 | 31 | 23 |
| ≥ 5 cm | 2.0 | 0.3 | 0.3 | 1.0 | 1.7 | 0.4 |
| Tromsø-test-3 (TM03) | | | | | | |
| < 1 cm | 46 | 65 | 70 | 61 | 53 | 65 |
| 1–5 cm | 47 | 33 | 30 | 36 | 42 | 33 |
| ≥ 5 cm | 7.5 | 2.0 | 0.6 | 3.4 | 6.0 | 1.8 |
| Tromsø-test-4 (TM04) | | | | | | |
| < 1 cm | 34 | 50 | 55 | 46 | 42 | 50 |
| 1–5 cm | 51 | 44 | 43 | 47 | 47 | 46 |
| ≥ 5 cm | 14.9 | 5.3 | 2.0 | 6.5 | 11.1 | 4.4 |
| Tromsø-test-5 (TM05) | | | | | | |
| < 1 cm | 32 | 45 | 52 | 44 | 40 | 46 |
| 1–5 cm | 54 | 49 | 46 | 49 | 49 | 49 |
| ≥ 5 cm | 14.7 | 6.1 | 2.3 | 6.7 | 10.4 | 5.0 |
| Simavika-monitor (MSIM) | | | | | | |
| < 1 cm | 31 | 41 | 44 | 37 | 34 | 41 |
| 1–5 cm | 52 | 53 | 55 | 55 | 53 | 54 |
| ≥ 5 cm | 16.9 | 5.5 | 1.5 | 8.1 | 12.5 | 4.2 |

**Table 3** Probability for vertical position noise

| std(pos) | Mag.Night | Mag.Dawn | Mag.Day | Mag.Dusk | Darkness | Sunlight |
|---|---|---|---|---|---|---|
| **Tromsø-monitor (MTRM)** | | | | | | |
| < 1 cm | 97 | 98 | 98 | 98 | 97 | 98 |
| 1–5 cm | 3 | 2 | 2 | 2 | 3 | 2 |
| ≥ 5 cm | 0.0 | 0.0 | 0.0 | 0.0 | 0.0 | 0.0 |
| **Tromsø-test-1 (TM01)** | | | | | | |
| < 1 cm | 31 | 60 | 68 | 51 | 38 | 61 |
| 1–5 cm | 63 | 39 | 32 | 46 | 57 | 37 |
| ≥ 5 cm | 5.7 | 1.1 | 0.4 | 3.0 | 4.5 | 1.4 |
| **Tromsø-test-3 (TM03)** | | | | | | |
| < 1 cm | 21 | 50 | 59 | 40 | 29 | 51 |
| 1–5 cm | 69 | 48 | 40 | 56 | 64 | 47 |
| ≥ 5 cm | 9.3 | 1.9 | 0.6 | 4.3 | 7.2 | 2.1 |
| **Tromsø-test-4 (TM04)** | | | | | | |
| < 1 cm | 18 | 40 | 45 | 29 | 27 | 38 |
| 1–5 cm | 71 | 57 | 53 | 65 | 65 | 59 |
| ≥ 5 cm | 11.4 | 3.5 | 1.5 | 5.6 | 8.2 | 3.6 |
| **Tromsø-test-5 (TM05)** | | | | | | |
| < 1 cm | 16 | 37 | 44 | 30 | 29 | 35 |
| 1–5 cm | 73 | 59 | 55 | 66 | 64 | 62 |
| ≥ 5 cm | 10.5 | 3.5 | 1.3 | 4.8 | 7.1 | 3.4 |
| **Simavika-monitor (MSIM)** | | | | | | |
| < 1 cm | 28 | 42 | 46 | 38 | 34 | 42 |
| 1–5 cm | 55 | 53 | 53 | 56 | 54 | 54 |
| ≥ 5 cm | 16.5 | 4.8 | 0.7 | 6.5 | 11.6 | 3.4 |

night-time occurrence of large coordinate errors from TM01 to TM05. The occurrence of large values of positioning noise exhibits a similar day/night difference, but does not appear to increase as rapidly with distance. The statistics for positioning disturbances sorted by the Sun being in view or not show similar behaviour, with significantly more disturbances during darkness than during sunlight, but with a lower ratio than when comparing the magnetic night and day. There is necessarily a large degree of correlation between these two ways of sorting the observations. The Fig. 7 provides a visualization of how the disturbances vary as a function of the time-of-day and year. This supports the conclusion that the time-of-day has a greater explanatory power than the amount of direct solar radiation, but that there is a semi-annual modulation of the level of activity and a possible modulation from the background ionization due to direct radiation.

Assumptions about normality of observations are commonly used in data analysis by the modeler and help to carry out the inference and hypothesis testing [35–37]. Most test statistics, for instance the Student *t*-test and Fisher *F*-test, rely on normality assumptions. Based on the results seen earlier, we suspect that data from disturbed periods will deviate from the Gaussian distribution.

To check this, we reconfigured one of the monitor receivers (TM05) to record coordinates at 1 s resolution without the periodic resets described in the introduction. This removes the ability to test the time-to-fix, but allows a better view of the distributions. With this configuration, a dataset of more than 1 month was recorded during 2022. No major events occurred during the measurement period. The dataset was split into 5 min length intervals and the distributions were analyzed to assess the deviation from the Gaussian distribution. Two representative examples of the results are included in this paper.

The normality detection indicator used in this investigation is the *p*-value of the test, which is defined as the observed significance level. A small value indicates there is a strong evidence for the alternative hypothesis $H_1$ and will lead to rejection of $H_0$. The $H_0$ hypothesis is that the data has a Gaussian distribution, while $H_1$ is the opposite. Mathematically, the p-value reads:

$$p = P(T \leq c_0 | H_0) \tag{2}$$

where $c_0$ is the observed value of the test statistics $T(\cdot)$, and $P(\cdot|H_0)$ denotes the probability under $H_0$. One major advantage of using *p*-value is that the hypothesis testing becomes very easy, because the probability tables are no

**Table 4** Probability for time-to-fix

| TTF | Mag.Night | Mag.Dawn | Mag.Day | Mag.Dusk | Darkness | Sunlight |
|---|---|---|---|---|---|---|
| **Tromsø-monitor (MTRM)** | | | | | | |
| < 10 s | 100 | 100 | 100 | 100 | 100 | 100 |
| 10–30 s | 0 | 0 | 0 | 0 | 0 | 0 |
| ≥ 30 s | 0.0 | 0.0 | 0.0 | 0.0 | 0.0 | 0.0 |
| **Tromsø-test-1 (TM01)** | | | | | | |
| < 10 s | 98 | 99 | 100 | 99 | 99 | 99 |
| 10–30 s | 1 | 1 | 0 | 1 | 1 | 0 |
| ≥ 30 s | 0.2 | 0.1 | 0.0 | 0.1 | 0.2 | 0.1 |
| **Tromsø-test-3 (TM03)** | | | | | | |
| < 10 s | 84 | 94 | 98 | 93 | 88 | 96 |
| 10–30 s | 13 | 5 | 2 | 5 | 10 | 4 |
| ≥ 30 s | 3.7 | 1.1 | 0.3 | 1.5 | 2.7 | 0.8 |
| **Tromsø-test-4 (TM04)** | | | | | | |
| < 10 s | 76 | 90 | 94 | 90 | 83 | 91 |
| 10–30 s | 18 | 8 | 5 | 8 | 13 | 7 |
| ≥ 30 s | 6.1 | 2.1 | 0.9 | 2.2 | 4.2 | 1.6 |
| **Tromsø-test-5 (TM05)** | | | | | | |
| < 10 s | 75 | 89 | 94 | 89 | 83 | 91 |
| 10–30 s | 19 | 9 | 5 | 8 | 13 | 7 |
| ≥ 30 s | 5.9 | 2.2 | 0.9 | 2.2 | 3.9 | 1.7 |
| **Simavika-monitor (MSIM)** | | | | | | |
| < 10 s | 83 | 95 | 99 | 93 | 89 | 96 |
| 10–30 s | 10 | 3 | 1 | 4 | 7 | 2 |
| ≥ 30 s | 6.4 | 1.7 | 0.3 | 2.6 | 4.4 | 1.3 |

longer necessary. The interested reader can find a procedure on how to compute the *p*-value for a specific test statistics $T(\cdot)$ in [38, p. 200]. Normality tests that can be used are:

- Jarque-Bera ($T_{JB}$): The Jarque-Bera normality test [39] uses the third and the fourth moments about the mean known as the skewness and kurtosis, respectively, to assess the deviation from normality.
- Kolmogorov-Smirnof($T_{KS}$): The empirical test statistic $D = T_{\mathbf{KS}}$ is based on the empirical distribution function (EDF). Kolmogorv–Smirnov test statistics are used to determine if the observations follow a certain distribution not just test for normality [40]. The interested reader of the original work of the Kolmogorov's 1933 paper is referred to [41].
- Shapiro and Shapiro-Francia ($T_{SF}$) normality test [42]
- Other test statistics can also be used. For instance; Anderson-Darling, Cramer-von Mises, and Pearson chi-square tests

All of these have been computed, and agree of the deviations from the Gaussian distribution, but in the example figures we only list the value of the Kolmogorov-Smirnof test. Figure 13 shows an example of good data, where the

Gaussian assumption is reasonable, while Fig. 14 shows an example of bad data, where the Gaussian assumption does not hold. The distributions are observed to deviate in several ways, including distributions with multiple peaks, asymmetric, not centered around zero, and with significantly longer tails (more extreme values). This can for example lead to erroneous results in integrity test, which in the worst case will fail to detect integrity violations.

## 5 Conclusions

In this study we have examined the performance of a NRTK positioning service at high latitudes ($\approx 70^o$ N), as a function of time-of-day and distance to the nearest NRTK receiver.

Ambiguities fixing performance is good at TM01 (1.2 km), but suffering at TM03 (5.3 km) and greater distances. At day-time the effect of increased time-to-fix is small, while at night it can reach tens of seconds.

Positioning biases and noise are increased at all distances tested from 1.2 km and greater. The increase in occurrence of large coordinate errors (> 5 cm) is

**Fig. 13** Distributions of coordinates based on 5 min of undisturbed data. Top panel shows the X coord. distribution along with a best fit of a zero-centered Gaussian. Middle and Bottom panel show the same, for the Y and Z coordinates
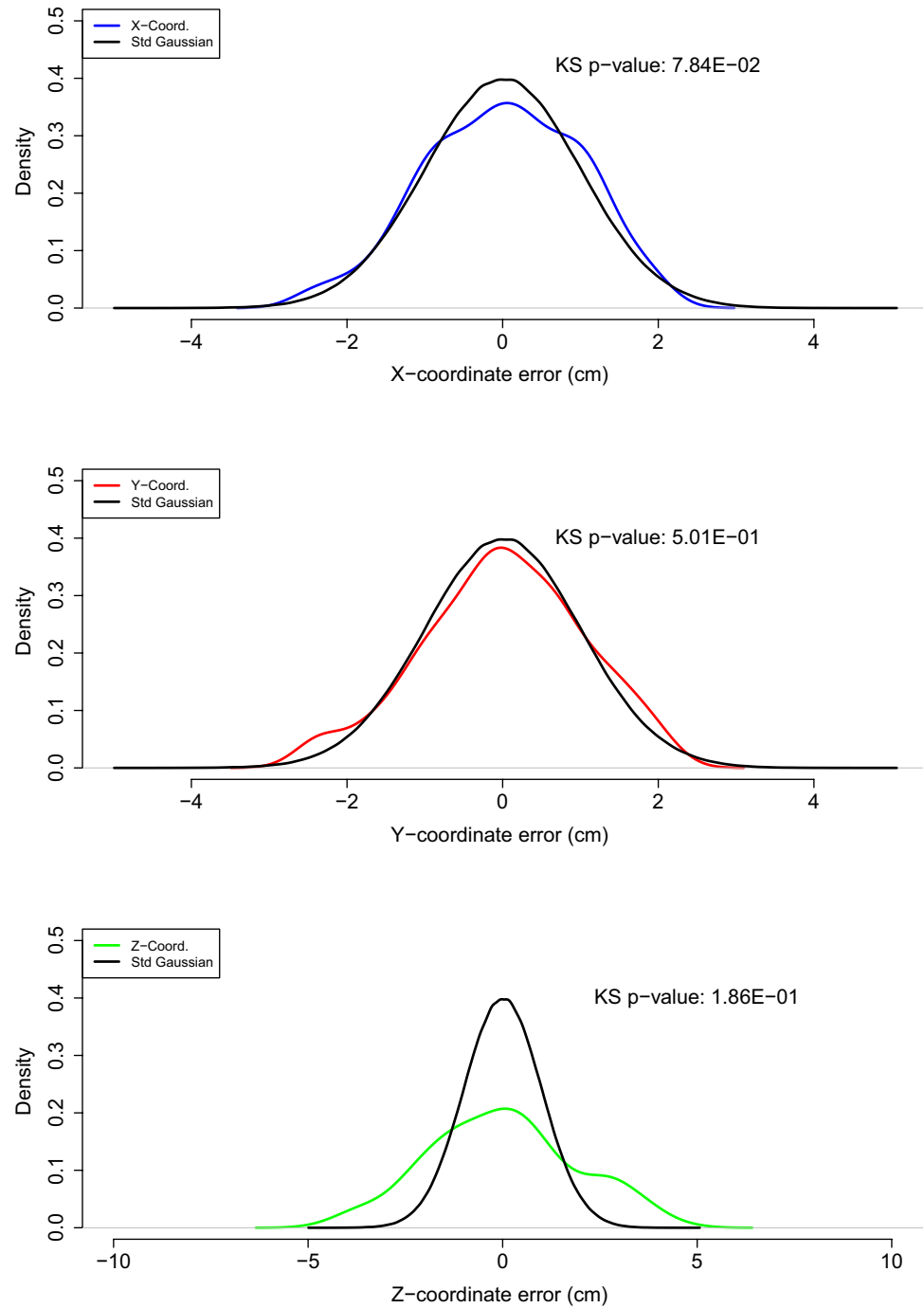


approximately ten-fold when comparing the monitor receiver at 1.2 km to the monitor receiver at 11.5 km.

During magnetic night-time there is a greatly enhanced risk that a single measurement will have a large error. The increase in occurrence of large coordinate errors is approximately ten-fold when comparing magnetic night-time to day-time.

We have observed signs of a semi-annual modulation of the level of disturbance, which may be explained by the "Russell-McPherron" effect.

The cause of the observed degradations are likely small-scale (few km or less) ionospheric density structures in the auroral oval region.

**Fig. 14** Distributions of coordinates based on 5 min of disturbed data. Top panel shows the X coord. distribution along with a best fit of a zero-centered Gaussian. Middle and Bottom panel show the same, for the Y and Z coordinates
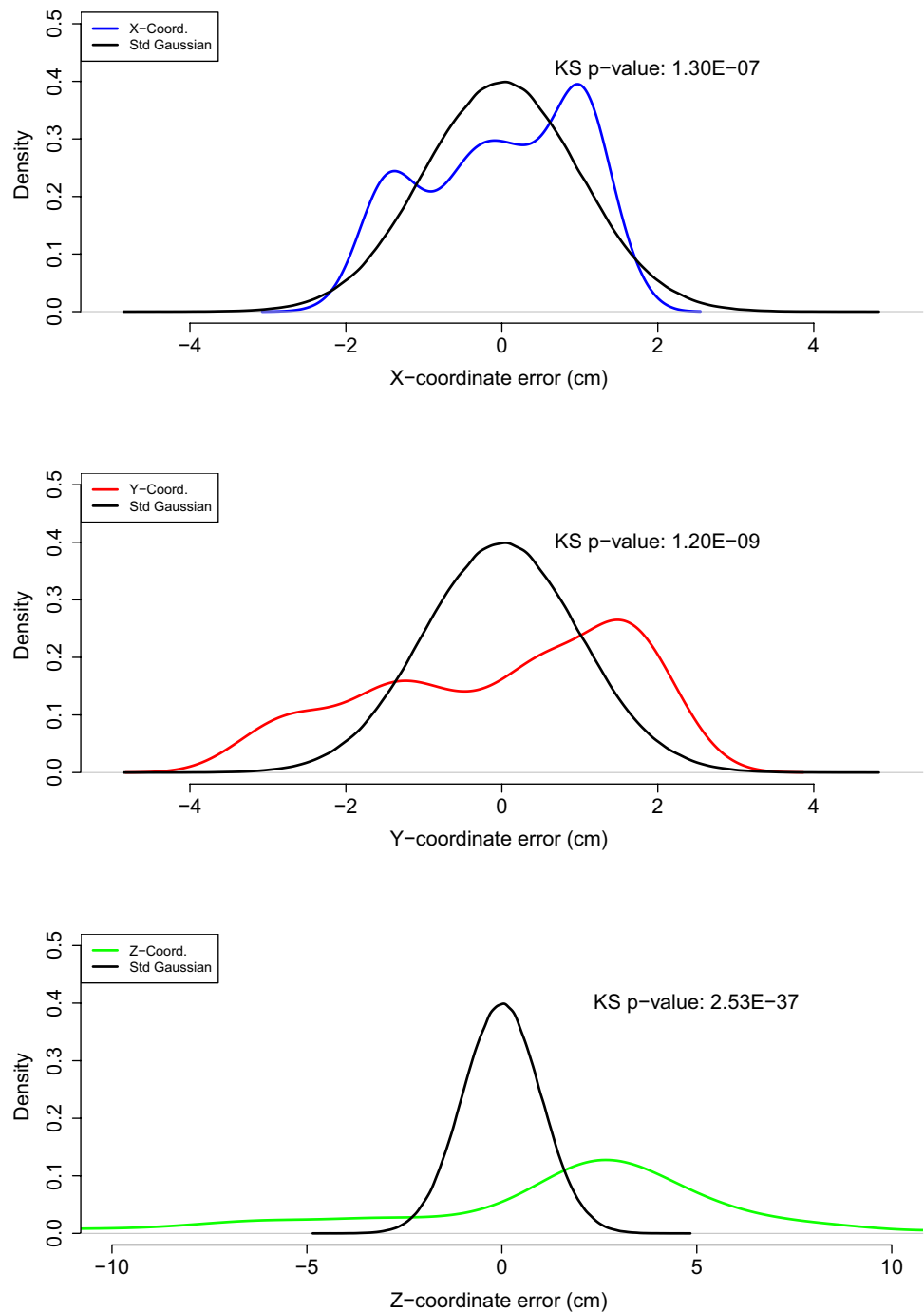


During disturbed periods, the distributions of the calculated coordinates are no longer following a Gaussian distribution. This can lead to misleading integrity information.

These data have been generated as described in Sect. 3. The full set of raw data files used in this study are available from the corresponding author on reasonable request.

## Declarations

# References

1. Frodge SL, Deloach SR, Remondi B, Lapucha D, Barker RA (1994) Real-time on-the-fly kinematic GPS system results. Navigation 41(2):175–186

2. Wübbena G, Bagge A, Seeber G, Boder V, Hankemeier P (1996) Reducing distance dependent errors for real-time precise dgps applications by establishing reference station networks. In: Proceedings of the 9th International Technical Meeting of the Satellite Division of The Institute of Navigation (ION GPS 1996), Kansas, pp. 1845–1852

3. Landau H, Vollath U, Chen X (2002) Virtual reference station systems. J Global Posit Syst 1:137–143. https://doi.org/10.5081/jgps.1.2.137

4. Rizos C (2003) Network RTK research and implementation: a geodetic perspective. J Global Posit Syst 1(2):144–150

5. Raquet JF (1998) Development of a method for kinematic gps carrier-phase ambiguity resolution using multiple reference receivers. PhD thesis, University of Calgary

6. Raquet J, Lachapelle G (1999) Development and testing of a kinematic carrier-phase ambiguity resolution method using a reference receiver network 1. Navigation 46(4):283–295. https://doi.org/10.1002/j.2161-4296.1999.tb02415.x

7. Dermanis A (1984) Kriging and collocation: a comparison. Manuscr Geod 9:159–167

8. Introduction to Least Squares Collocation and the Kriging Methods, pp. 613–633. Wiley (2018). Chap. 16. https://doi.org/10.1002/9781119501459.ch16. https://onlinelibrary.wiley.com/doi/abs/10.1002/9781119501459.ch16

9. Ligas M (2022) Comparison of kriging and least-squares collocation-revisited. J Appl Geod 16(3):217–227. https://doi.org/10.1515/jag-2021-0032

10. El-Mowafy A (2012) Precise real-time positioning using network rtk. In: Jin, S. (ed.) Global navigation satellite systems. IntechOpen, Rijeka. Chap. 7. https://doi.org/10.5772/29502

11. Jacobsen KS, Dähnn M (2014) Statistics of ionospheric disturbances and their correlation with GNSS positioning errors at high latitudes. J Space Weather Space Clim 4:27. https://doi.org/10.1051/swsc/2014024

12. Jacobsen KS, Schäfer S (2012) Observed effects of a geomagnetic storm on an RTK positioning network at high latitudes. J Space Weather Space Clim 2:13. https://doi.org/10.1051/swsc/2012013

13. Andalsvik YL, Jacobsen KS (2014) Observed high-latitude GNSS disturbances during a less-than-minor geomagnetic storm. Radio Sci 49(12):1277–1288. https://doi.org/10.1002/2014RS005418

14. Jacobsen KS, Andalsvik YL (2016) Overview of the 2015 st. Patrick's day storm and its consequences for RTK and PPP positioning in Norway. J Space Weather Space Clim 9:6. https://doi.org/10.1051/swsc/2016004

15. Janssen V, Haasdyk J (2011) Assessment of network rtk performance using corsnet-nsw. In: Proceedings of IGNSS 2011 Symposium, Sydney

16. Gumilar I, Bramanto B, Rahman FF, Hermawan IM (2019) Variability and performance of short to long-range single baseline RTK GNSS positioning in Indonesia. E3S Web Conf 94:01012. https://doi.org/10.1051/e3sconf/20199401012

17. Shu B, Liu H, Xu L, Qian C, Gong X, An X (2018) Performance analysis of BDS medium-long baseline RTK positioning using an empirical troposphere model. Sensors 4:18. https://doi.org/10.3390/s18041199

18. Alkan RM, Ozulu IM, Ilci V (2017) Performance evaluation of single baseline and network RTK GNSS. Coordinates. Accessed 07 March 2022

19. Gökdaş O, Özlüdemir MT (2020) A variance model in NRTK-based geodetic positioning as a function of baseline length. Geosciences 7:10. https://doi.org/10.3390/geosciences10070262

20. Wübbena G, Bagge A (2002) Rtcm message type 59-fkp for transmission of fkp. Geo++ White Paper

21. Öğütcü S (2017) İbrahim Kalaycı: investigating precision of network based RTK techniques: baseline length is concerned. World J Res Rev (WJRR) 5:01–03

22. Bisai N, Sen A (2021) Physical origin of short scale plasma structures in the auroral f region. J Geophys Res 126(3):2020. https://doi.org/10.1029/2020JA028422

23. Gondarenko NA, Guzdar PN (2006) Nonlinear three-dimensional simulations of mesoscale structuring by multiple drives in high-latitude plasma patches. J Geophys Res 8:111. https://doi.org/10.1029/2006JA011701

24. Keskinen MJ, Ossakow SL (1983) Nonlinear evolution of convecting plasma enhancements in the auroral ionosphere: 2. small scale irregularities. J Geophys Res 88:474–482. https://doi.org/10.1029/JA088iA01p00474

25. Zettergren MD, Semeter JL, Dahlgren H (2015) Dynamics of density cavities generated by frictional heating: formation, distortion, and instability. Geophysical Res Lett 42(23):10120–10125. https://doi.org/10.1002/2015GL066806

26. Spicher A, Deshpande K, Jin Y, Oksavik K, Zettergren M, Clausen LBN, Moen JI, Hairston MR, Baddeley L (2020) On the production of ionospheric irregularities via kelvin-helmholtz instability associated with cusp flow channels. J Geophys Res 125(6):2019. https://doi.org/10.1029/2019JA027734

27. Xiong C, Yin F, Luo X, Yaqi J, Wan X (2019) Plasma patches inside the polar cap and auroral oval: the impact on the spaceborne GPS receiver. J Space Weather Space Clim 9:25. https://doi.org/10.1051/swsc/2019028

28. Spicher A, LaBelle J, Bonnell JW, Roglans R, Moser C, Fuselier SA, Bounds S, Clausen LB, Di Mare F, Feltman CA, Jin Y (2017) GPS scintillations associated with cusp dynamics and polar cap patches. J Space Weather Space Clim 23:7. https://doi.org/10.1051/swsc/20170222017

29. van devan der Meeren C, Oksavik K, Lorentzen D, Moen JI, Romano V (2014) Gps scintillation and irregularities at the front of an ionization tongue in the nightside polar ionosphere. J Geophys Res 119(10):8624–8636. https://doi.org/10.1002/2014JA020114

30. Dach R, Lutz S, Walser P, Fridez P (2018) Bernese GNSS Software Version 5.2. https://doi.org/10.7892/boris.72297. User manual of the Bernese GNSS Software, Version 5.2. https://boris.unibe.ch/id/eprint/72297

31. PROJ contributors: PROJ Coordinate Transformation Software Library. Open Source Geospatial Foundation (2022). https://doi.org/10.5281/zenodo.5884394. Open Source Geospatial Foundation. https://proj.org/

32. Jung S, Lee J (2012) Long-term ionospheric anomaly monitoring for ground based augmentation systems. Radio Sci 47(04):1–12. https://doi.org/10.1029/2012RS005016

33. Robert E, Jonas P, Vuillaume J, Salos D, Hecker L, Yaya P (2018) Development of a European ionosphere threat model in support of GBAS deployment. In: 2018 IEEE/ION Position, Location and Navigation Symposium (PLANS), Monterey, pp. 1181–1190

34. Russell CT, McPherron RL (1973) Semiannual variation of geomagnetic activity. J Geophys Res 78(1):92–108. https://doi.org/10.1029/JA078i001p00092

35. Brown RG (1992) A baseline GPS RAIM scheme and a note on the equivalence of three RAIM methods. Navigation 39(3):301–316. https://doi.org/10.1002/j.2161-4296.1992.tb02278.x

36. Li L, Quddus M, Ison S, Zhao L (2012) Multiple reference consistency check for LAAS: a novel position domain approach. GPS Solut 16:209–220. https://doi.org/10.1007/s10291-011-0223-y

37. Zhao L, Zhang J, Li L, Yang F, Liu X (2020) Position-domain non-gaussian error overbounding for ARAIM. Remote Sens 2:12. https://doi.org/10.3390/rs12121992

38. Martinez WL, Martinez AR (2001) Computational statistics handbook with MATLAB. CRC Press, Boca Raton

39. Jarque CM, Bera AK (1987) A test for normality of observations and regression residuals. Int Stat Rev 55(2):163–172. https://doi.org/10.2307/1403192

40. Ouassou M (2018) Implementation of GNSS data integrity for precise real-time positioning. PhD Thesis, Norwegian University of Life Sciences, Faculty of Science and Technology (REALTEK)

41. Stephens MA (1992) An appreciation of Kolmogorov's 1933 paper. Defense Technical Information Center,. https://books.google.no/books?id=DceLPwAACAAJ

42. Sarkadi K (1975) The consistency of the Shapiro–Francia test. Biometrika 62(2):445–450